



Citlalmitl: A Laser-based Device for Meteoritical Sample Fabrication with Arbitrary Thermal Histories

Patricia Hernández-Reséndiz¹ , Héctor Cruz-Ramírez¹, Alfred B. U'Ren¹ , Karina Elizabeth Cervantes-de la Cruz² , and Antígona Segura¹ 

¹ Instituto de Ciencias Nucleares, Universidad Nacional Autónoma de México, Mexico; patricia.hernandez@correo.nucleares.unam.mx

² Departamento de Física, Facultad de Ciencias, Universidad Nacional Autónoma de México, Mexico

Received 2020 January 14; revised 2020 July 3; accepted 2020 July 6; published 2020 August 14

Abstract

We present Citlalmitl (the word for meteorite in the Nahuatl language), a new experimental device designed and built to simulate high-temperature processes relevant for meteoritics, including chondrule formation and the atmospheric entry of micrometeorites (MMs). The main component of Citlalmitl is a 50 W CO₂ laser, used to melt samples that simulate the precursors of meteoritical materials. As examples of the operation of our device, we have irradiated silicate samples controlling the laser duty cycle to reproduce heating profiles predicted by shock-wave simulations. Citlalmitl records the sample temperature during and after irradiation, a unique feature that allows us to directly measure the thermal history of the sample, a key parameter for the characteristics observed in MMs and chondrules. We demonstrate that Citlalmitl can reproduce different heating profiles useful to mimic thermal histories in meteoritical processes.

Unified Astronomy Thesaurus concepts: [Astronomical instrumentation \(799\)](#); [Meteorites \(1038\)](#); [Micrometeorites \(1047\)](#); [Chondrules \(229\)](#)

1. Introduction

Lasers have multiple applications in geophysical and planetary chemistry research. For example, they have been used to simulate sources of energy for prebiotic chemistry experiments (e.g., Scattergood et al. 1989; Ferus et al. 2015), lightning and atmospheric chemistry driven by lightning (e.g., Borucki et al. 1985, 1988; Mvondo et al. 2001; Ramírez et al. 2005), and astronomical jets (e.g., Villagran-Muniz et al. 2003). In the area of meteoritics, lasers are used to reproduce high-energy processes such as chondrule formation and atmospheric entry of micrometeorites. Chondrules are millimeter-scale silicate melted spherules that represent the main component of chondritic meteorites, the oldest rock samples among meteorites; they have been found in comets (e.g., Nakamura et al. 2008). While their characteristics imply formation at peak temperatures between 1400 and 2100°C (e.g., Ciesla 2005; Scott 2007) our understanding of their formation mechanisms remains elusive. Micrometeorites (MMs) are melted or unmelted particles, with dimensions between 10 μm and 2 mm, found on our planet's surface, originated from comets and main-belt asteroids although their exact sources have not been fully determined (e.g., Battandier et al. 2018). Both, chondrules and MMs represent key components for understanding the evolution of our solar system. Here, we present a new experimental device, Citlalmitl (the word for meteorite in the Nahuatl language), designed and built to simulate high-temperature processes relevant for meteoritics, which can be adapted for other purposes such as shock-wave experiments.

1.1. Chondrules

The oldest meteorites are the undifferentiated meteorites, or chondrites. They were formed by accretion of the original material of the protoplanetary disk so that they preserve the oldest components of the solar system. Chondrules are the major components of chondrites; they constitute up to 80% by volume of ordinary and enstatite chondrites, while they constitute around 40% by volume of carbonaceous chondrites (Weisberg et al. 2006). The mean chondrule diameter for different chondrite groups ranges from 0.2 to 1 mm (Jones 2012). They are largely composed of olivine (Mg_xFe_{1-x})₂SiO₄, low-Ca pyroxene, Mg_xFe_{1-x}SiO₃ (where x is the Mg/(Mg+Fe) ratio), mesostasis, and assemblages such as Fe-Ni alloy and sulfides (Soulié et al. 2017). Chondrules are thought to have crystallized on a timescale of minutes to hours (Scott 2007). Nowadays, there are many measurements of forsterite and enstatite in protoplanetary disks that indicate a sufficient abundance of these crystalline materials so as to consider them to be the principal precursors for chondrules (Oliveira et al. 2011; Sturm et al. 2013).

Chondrules are common and can have different textural types: granular, barred, radial, cryptocrystalline, and porphyritic (Gooding & Keil 1981; Lauretta et al. 2006). Porphyritic chondrules contain large crystals set in a fine-grained or glassy mesostasis, and are classified as dominated by olivine (PO), by pyroxene (PP), or by both (POP). Granular chondrules contain many small grains, also classified as: dominated by olivine (GO), by pyroxene (GP), and by both (GOP) groups. Barred olivine chondrules (BO) contain large and skeletal crystals. Radial pyroxene chondrules (RP) contain a fan-like array of low-Ca pyroxene. Cryptocrystalline chondrules have a high abundance of glassy material and do not exhibit a recognizable crystal structure.

Some important unknowns in the formation of chondrules are (Ciesla 2005): the composition of precursors, the physical conditions of their formation: pressure, temperature, and



Original content from this work may be used under the terms of the [Creative Commons Attribution 4.0 licence](#). Any further distribution of this work must maintain attribution to the author(s) and the title of the work, journal citation and DOI.

timescale, and the mechanisms that produce them; the best accepted model is based on shock waves (e.g., Desch & Connolly 2002). Two of the main properties of chondrules are: (i) the retention of volatile materials (e.g., Na, K, FeS), which do not survive heating and/or cooling for long periods of time (Hewins et al. 1996), and (ii) the existence of relict grains within some chondrules and composed chondrules indicating different heating events, instead of monotonic cooling after a single heating event (Ciesla 2005). The above suggests that the formation process was recurring in the first few million years of the solar system and that a material recycling process may have occurred in the formation regions (Jones 2012).

With our new device, Citlalmitl, we have fabricated chondrule analogs with the purpose of studying the chondrule formation processes (McSween 1977; Gooding & Keil 1981; Scott & Taylor 1983; Jones 1994) as well as their physical and chemical characteristics leading to constraints on the precursor composition, as well as on the heating and cooling rates during formation.

1.2. Micrometeorites

Micrometeorites (MMs) are naturally occurring solid objects between 10 μm and 2 mm in diameter (Rubin & Grossman 2010). They constitute space material directly available on Earth, which can help us to understand the composition and evolution of the materials from which our solar system was formed (e.g., Genge et al. 1997; Nesvorný et al. 2010; Engrand et al. 2016). There is general agreement that these materials originated from comets and main-belt asteroids, either from particles that result from collisions or from spontaneous comet disruptions, although the contribution of each source is still under debate (e.g., Gounelle et al. 2009; Badjukov et al. 2010; Nesvorný et al. 2010; Engrand et al. 2016; Battandier et al. 2018). Micrometeorites show a wide variety of compositions, some of them not represented in meteorite collections (e.g., Genge et al. 1997; Gounelle et al. 2009), making them an important element in our quest to understand the composition of the early solar system and its chemical and physical evolution. Nevertheless, melting during atmospheric entry can substantially alter the original composition of the resulting micrometeorites and these changes depend on several parameters such as entry velocity, density, mass, entry angle, and initial composition. Models and experiments are required to understand how thermal processes modify the components of these particles.

The MM classification was developed by Genge and collaborators based on their mineralogy. S-type MMs (silicate cosmic spherules) represent around 97% of those found in MM collections. They are thought to have reached peak temperatures of 1350–2000 °C (Genge et al. 2008) during formation, with olivine as the major silicate in their composition. The different subclasses are based on their resulting textures derived from their temperature histories and their mineralogy. Some of the subclasses are glass spherules (V), cryptocrystalline (CC), barred (B), and porphyritic. V spherules consist almost entirely of glass, CC spherules are dominated by submicron crystallites and magnetite, barred olivine (BO) are spherules dominated by parallel growth olivine within glass, and porphyritic olivine (PO) are spherules dominated by equant and skeletal olivine within glass. Note that all of these various types of MMs can present relict grains.

We explore the products of possible precursor grains during atmospheric entry by melting grains with the laser on which Citlalmitl is based and fabricate MM analogs to provide additional elements for the identification of new MM samples and to understand the role of the material precursor in the observed characteristics of the retrieved samples. Particularly, we can analyze the distribution of iron after irradiation, as related to the process of general mass loss.

1.3. High-temperature Experiments for Meteoritics

While it is common to use a furnace to form MM and chondrule analogs (e.g., Tsuchiyama et al. 1980; Tsuchiyama & Nagahara 1981; Hewins et al. 1989; Lofgren 1989; Lofgren & Lanier 1990; Greshake et al. 1998; Toppani et al. 2001, 2003), lasers have proven for melting samples that reproduce the characteristics of chondrules (e.g., Nelson et al. 1972; Blander et al. 1976; Eisenhour et al. 1994; Nagashima et al. 2006) and MMs (Kaluna et al. 2017). Poppe et al. (2010) reported the advantages of employing laser irradiation to melt aggregates of silicate grains because lasers can simulate radiative heating of whatever origin, including lightning and shock waves. This last option represents the best accepted candidate mechanism for chondrule formation nowadays. They found that it is a more efficient technique in the production of molten spheres with dimensions similar to chondrules and MMs, as compared with melting by electric-discharge heating, indicating that the energetic efficiency is better by orders of magnitude. Another specific advantage of the laser-irradiation technique is that it permits accurate control of the heating and cooling rates, which is crucial in order to reproduce likely formation conditions for chondrules (Desch et al. 2012) and the entry heating of MMs (Toppani et al. 2001; Genge 2017).

We irradiated silicate grains with the beam from a 50 W CO₂ laser (SYNRAD 48-5) in order to reproduce temperatures, cooling rates, and mass losses predicted for the natural forming processes of MMs and chondrules (Briani et al. 2013; Rudraswami et al. 2016b, 2016a). We chose the CO₂ laser operating at a wavelength of 10.6 μm because silicates are good absorbers at this wavelength (Farmer 1976; Bowey et al. 1998; Ostrooumov 2007) and it is commonly used for heating silicates (e.g., York et al. 1981; Nordine & Atkins 1982; Solé 2009; Zhu et al. 2020).

2. Citlalmitl: Meteorite Fabrication

The diagram of the experimental device, or Citlalmitl, is shown in Figure 1. Citlalmitl consists of a steel vacuum chamber (VC), equipped with a sample holder (A) in the chamber interior. A ZnSe main porthole on the top surface of the VC permits a beam from a 50 W CO₂ laser operating at a wavelength of 10.6 μm to reach the sample holder. Thus, the laser beam, which can be adequately modeled as a Gaussian beam, is used as a heat source for the controlled melting of the silicates.

This experimental device, Citlalmitl, was specially designed with the purpose of reproducing the conditions and the thermal histories predicted by the chondrule formation models and MM entry models to evaluate them with better accuracy. For this reason, Citlalmitl is able to heat samples with different irradiation temporal profiles, which will be described below.

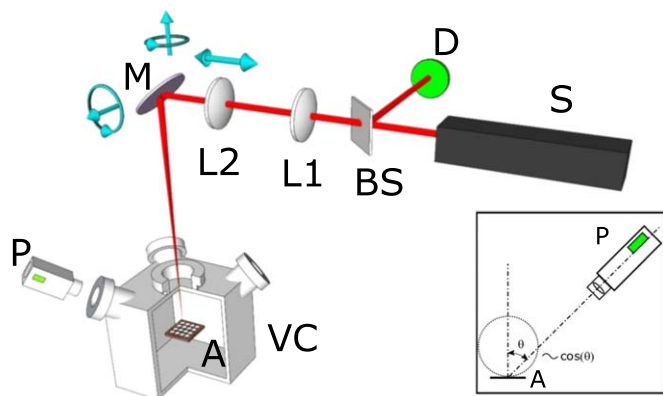


Figure 1. Diagram of Citlalmitl, the experimental device. S = CO_2 laser, D = power detector, BS = beamsplitter 95:5, $L1$ = static lens ($f = 50$ mm), $L2$ = motorized lens ($f = 200$ mm), M = mirror, A = sample holder, VC = vacuum chamber, and P = pyrometer. The four lateral portholes are not shown in the figure, but one is used as gate to introduce samples, the other two are connected to the vacuum pump, and the last one is sealed off. Bottom right: sample holder and pyrometer placement; as an approximation, we assume that the emission obeys Lambert's law, so that a temperature correction is required to account for the angular placement of the pyrometer at $\theta = 45^\circ$.

2.1. Confinement

The cube-shaped steel vacuum chamber (VC) has a volume of $27,000 \text{ cm}^3$. As already mentioned, the main ZnSe porthole on the chamber's top surface allows the laser beam to reach the sample holder. The chamber has a total of eight secondary portholes, meant for various diagnostic measurements, three of which are currently sealed off. The first secondary porthole leads to a vacuum turbo-pump (Pfeiffer Vacuum Hi-Cube 80 Eco) to reduce the pressure in the chamber as required. A second porthole permits the measurement of the chamber pressure using a Pfeiffer vacuum pressure gauge. A third porthole, covered with a borosilicate glass window (opaque for far- and mid-IR) permits visual monitoring of the samples using a visible-light CCD camera; a fourth porthole, also covered with a borosilicate glass window, permits monitoring of the sample temperature, relying on a variable-orientation pyrometer (LumaSense Impac 140 (P)). It is important to point out that the vacuum chamber serves the important purpose of maintaining the samples free from contaminants and protecting the experimenters from the laser beam.

A sample holder (A) contains a 6×6 array of semi-spherical depressions designed to hold the precursor material roughly in the center of the vacuum chamber. We use two different sample-holder plates: the first one is made from steel and has 18 depressions with a 3 mm diameter, and the remaining 18 with 4 mm diameter, while the second one is made from high-purity copper with all its 36 depressions of 3.4 mm diameter. These materials were chosen because they do not react chemically with the various gases that may be produced during irradiation and are thermally conductive, allowing for the dissipation of thermal energy resulting from the laser irradiation of the samples. Note that prior to our experimental runs, the thermal conductivity of both sample-holder plates was tested through laser irradiation while recording their temperature with the pyrometer. For both sample holders, the pyrometer did not at any point reach temperatures higher than 300°C , the lowest value that can be measured with the pyrometer (P).

2.2. High-precision Positioning

In our experiments it is crucial to be able to direct the laser beam to any of the 36 depressions in the sample holder. This is achieved by reflecting a guide laser and, consequently, the CO_2 beam from a mirror, which is mounted on a computer-controlled motorized mirror holder. To determine the angular orientation of the mirror at any given time, we use a closed-loop system based on a pair of encoders mounted on the two linear piezoelectric actuators which control the mirror's tilt. We point the guide laser to the selected semi-spherical depression before the irradiation begins, and leave the orientation fixed for the entire duration of the irradiation process (for that particular depression).

2.3. Energy Control

As has been determined in previous works, silicates can be heated and melted reliably with a CO_2 gas laser beam (York et al. 1981; Nordine & Atkins 1982; Solé 2009; Zhu et al. 2020). We use a 50 W CO_2 laser beam (SYNRAD 48-5) emitting in the infrared, at $10.6 \mu\text{m}$. In order to control the optical intensity reaching the sample holder, we make use of our ability to control the laser power by setting its duty cycle, on the one hand, and the spot area, on the other hand. First, applying a periodic intensity modulation, at a repetition rate of 5, 10, or 20 kHz, controls the laser power so that the output power is proportional to the duty cycle (defined as the percentage of the modulation period during which the laser output is active; see Figure 2). We use the 95:5 beamsplitter to deviate a portion of the optical power to be monitored through a power meter. Second, in order to control the spot size diameter ($2W_0$) on the sample holder plane, the laser beam is transmitted through an optical system composed of two ZnSe lenses with focal lengths of 50 mm ($L1$) and 200 mm ($L2$) forming a telescope, the second of which is displaceable with a stepper motor ($100 \mu\text{m}$ minimum step and 25 mm travel). This results in our capability to vary the spot size radius W_0 on the sample holder plane between 0.5 mm and 1.15 mm (Figure 3), or to set it to a value of 1.75 mm without the use of the telescope, as determined by a knife-edge test.

Our ability to control the laser power (through the variation of the duty cycle between 0 and 95%) as well as the spot size area, permits us to vary the optical intensity between 2 W cm^{-2} and $7 \times 10^3 \text{ W cm}^{-2}$. With this system, we are able to reach sufficiently high temperatures for the melting of silicates. We characterize the power losses at each step of the optical path. The laser response time, to increase the output power by 1W, is around ~ 100 ms; i.e., the laser does not respond instantaneously to changes in the operation parameters made at the laser controller.

2.4. Parameter Measurement

Citlalmitl is installed in a laboratory with the humidity maintained at a constant level of $30 \pm 1\%$ and the room temperature maintained at $19 \pm 1^\circ\text{C}$. The pressure in the vacuum chamber is monitored with the help of a Pfeiffer vacuum pressure gauge connected to the vacuum turbo-pump Pfeiffer Vacuum Hi-Cube 80 Eco. Depending on the experiments to be performed, the chamber can be used at atmospheric pressure (0.76 atm in Mexico City), or its pressure can be brought reduced to levels down to 10^{-5} atm.

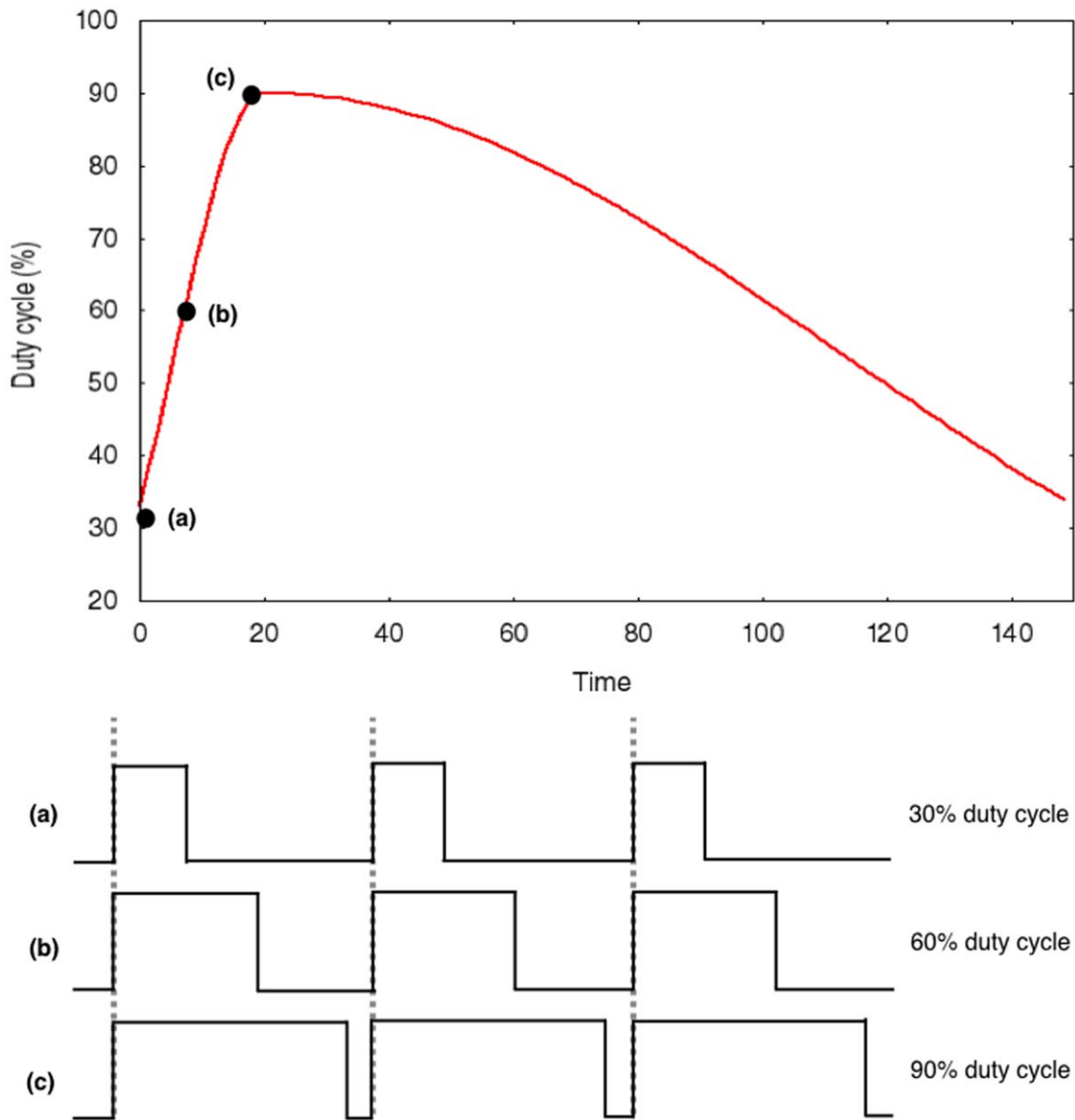


Figure 2. Duty cycle of the laser is the percentage of the modulation period during which the laser output is active. The units for the time axis are seconds.

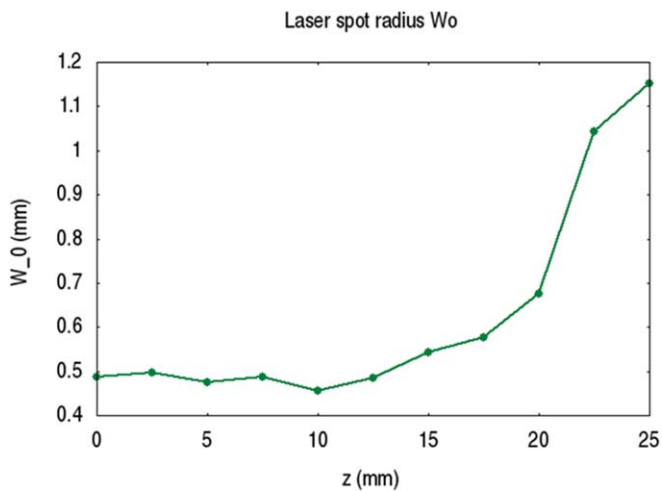


Figure 3. Variation of the spot size radius W_0 with the displacement of L2.

We record the temperature of our samples with the help of a pyrometer Lumasense IMPAC 140P during and after each melting process. Note that the laser radiation cannot reach the pyrometer since the window used in the corresponding port is not transparent to the laser wavelength of $10.6 \mu\text{m}$. Background radiation reaching the pyrometer is suppressed using a cylindrical shield, which restricts its angular acceptance. In this manner, we record directly in situ the thermal history for each sample, pointing it manually to each semi-spherical depression. While the pyrometer is designed to measure at normal incidence, in our experimental arrangement it is located outside the vacuum chamber at an orientation of 45° with respect to the incoming laser beam (inset in Figure 1). Assuming Lambertian emission from our samples during irradiation, the emission has an angular dependence proportional to $\cos \theta$, leading to a necessary temperature measurement correction to be made during data processing. We confirmed this $\cos \theta$ dependence by making measurements with a source

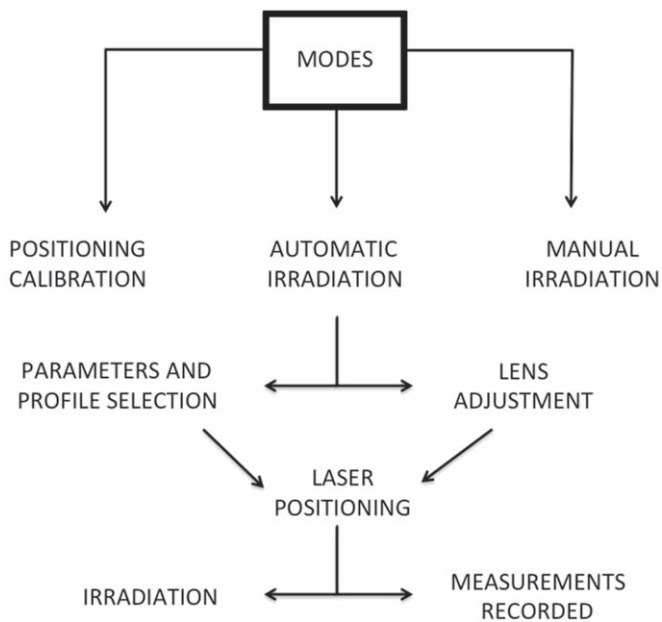


Figure 4. Flow chart of the Citlalmitl control program in *LabView*.

with known temperature while varying the angle of orientation of the pyrometer.

2.5. Automation and Control

Citlalmitl, including all of its constituent instruments, is controlled with a single master experiment interface programmed with *LabView*, which directs the irradiation process (Figure 4):

1. The angular position of the mirror (M) required to reach any of the 36 depressions in the sample holder is previously calibrated through the high-precision encoders in the linear actuators, so that we can instruct Citlalmitl to direct the laser power to any one of them.
2. The spot size diameter ($2W_0$) on the sample holder plane can be controlled through the computer-controlled displacement of lens L2.
3. The laser power can be controlled through the laser's duty cycle, so that by varying the duty cycle during the course of an experimental run it becomes possible to determine the thermal history of a given sample, to be verified through the temperature measurement of the sample versus time with the pyrometer (see Figure 5).
4. For each experimental run, we record the laser power versus time as well as the resulting sample temperature versus time dependence.

3. Experiments

3.1. Properties of Precursors

Olivine grains were used, so as to determine whether Citlalmitl can efficiently melt one of the main minerals found in chondrules and MMs. We then added feldspar grains as a second, more realistic precursor composition for chondrules and MMs (e.g., Hewins & Fox 2004; Brownlee et al. 1983).

The olivine crystals used as precursor material have a density of 3.27 g cm^{-3} . They were crushed and separated into fractions of diameter $212 \mu\text{m} < d < 250 \mu\text{m}$, $250 \mu\text{m} < d < 300 \mu\text{m}$,

$300 \mu\text{m} < d < 500 \mu\text{m}$, and $d > 500 \mu\text{m}$. In those cases for which the initial material is in the form of a single grain, we measured its diameter with the help of image processing software. The initial sample masses are in the range of 0.12–2.2 mg.

The olivine composition was analyzed by means of X-ray fluorescence. The average content of forsterite ($\text{Fo} = \text{Mg}/(\text{Mg} + \text{Fe})$) is 91.6 mol% and the chemical composition is $\text{Mg}_{1.8}\text{Fe}_{0.2}\text{SiO}_4$, as seen in Table 1, similar to that used in Cervantes-de la Cruz (2009) and Cervantes-de la Cruz et al. (2015), so as to reproduce chondrule analogs. The calculated melt temperature is 1400°C (1673 K).

The feldspar grains used as precursor material for some of our samples were crushed and used in the diameter range of $125 \mu\text{m} < d < 250 \mu\text{m}$. The initial sample masses are in the range of 0.1–0.3 mg. The feldspar composition was analyzed by means of X-ray fluorescence and is shown in Table 2. The average content of albite ($\text{Ab} = \text{Na}/(\text{K} + \text{Na} + \text{Ca})$) is 29.9 mol%, that of anorthite ($\text{An} = \text{Ca}/(\text{K} + \text{Na} + \text{Ca})$) is 2.5 mol%, and that of orthoclase ($\text{Or} = \text{K}/(\text{K} + \text{Na} + \text{Ca})$) is 67.5 mol%.

3.2. Experimental Procedure

The weight of each sample is measured before and after the irradiation by means of an analytical scale (Ohaus Analytical Plus) with an accuracy of $\pm 0.005 \text{ mg}$, with the purpose of evaluating mass loss. Depending on the conditions to be tested, we place either one or a few grains of a given size range described in Section 3.1 in each depression of the sample holder (Table 3). Samples do not need any other preparation prior to being irradiated. Thus, after weighing the samples, the loaded sample plate is introduced into the vacuum chamber where the samples are irradiated by the laser beam, using a given choice of heating and cooling conditions (Figure 5).

The sample temperature and the laser power are recorded during and after irradiation until the analog cools below the detection threshold of the pyrometer (300°C).

A certain level of evaporation occurs in the precursor grains during the irradiation and leads to mass loss. This evaporated material condenses nearby the same sample and cross-contamination between semi-spherical depressions in the sample holder is definitely a possibility. However, after each experimental run we visually inspected the spaces between semi-spherical depressions and verified that the amount of leftover material was negligible.

After the analog's formation, we perform petrologic, chemical, and textural analysis with a stereoscopic microscope, an electronic variable scanning microscope, and an electron probe microanalyzer, respectively. These sample characterization tests are carried out so as to evaluate whether the analogs exhibit known chondrule and MM characteristics.

3.3. Experimental Profiles

A number of temperature profiles have been proposed, derived from different formation models for chondrules and entry models for MMs in literature (Desch & Connolly 2002; Desch et al. 2012; Rudraswami et al. 2016a). In order to simulate chondrule formation scenarios (Desch et al. 2012) and MM atmospheric entry scenarios (Rudraswami et al. 2016a), we create two different types of laser power modulation profiles, to be referred to as profiles A and B.

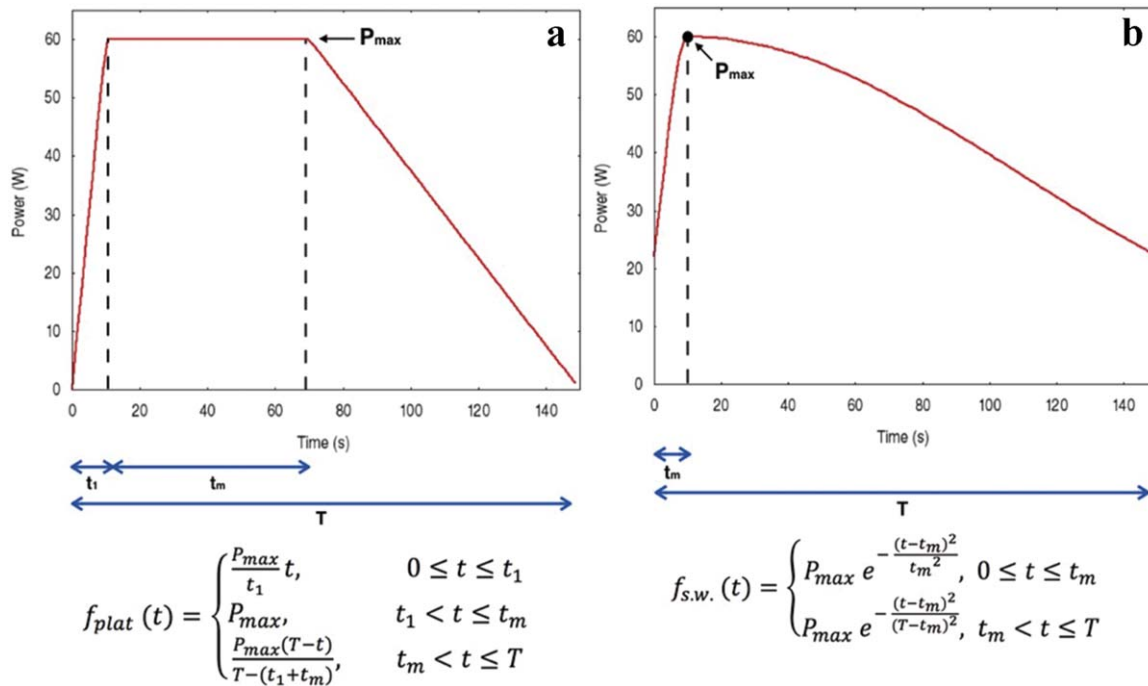


Figure 5. (a) Plateau irradiation profile, referred to as profile A. (b) Shock-wave irradiation profile, referred to as profile B. Underneath the plots we present the formulas that define these profiles.

Table 1
Chemical Composition of the Olivine Precursor Material

| Sample Oxide | Olivine Precursor (wt %) | Cations Calculated based on 4 Oxygen Atoms | |
|--------------------------------|--------------------------|--|------|
| SiO ₂ | 40.43 | Si | 0.99 |
| Al ₂ O ₃ | 0.23 | Al | 0.01 |
| MnO | 0.12 | Mn | b.d. |
| MgO | 49.74 | Mg | 1.81 |
| Fe ₂ O ₃ | 1.01 | Fe+3 | 0.02 |
| FeO | 8.13 | Fe | 0.17 |
| NaO | 0.01 | Cr | b.d. |
| Cr ₂ O ₃ | 0.03 | Ca | b.d. |
| CaO | 0.09 | Ti | b.d. |
| TiO ₂ | 0.01 | | |
| K ₂ O | 0.01 | | |
| P ₂ O ₅ | 0.01 | | |
| NiO | 0.15 | | |
| Total | 99.99 | Total | 3.00 |
| | | Fo % | 91.6 |
| | | Fa % | 8.4 |

Note. Obtained by X-ray fluorescence by Cervantes-de la Cruz (2009); b. d. = below detection limit.

Profile A has a plateau shape, with comparatively short rise and fall times (Figure 5(a)), which can reproduce rapid heating and cooling and the constant application of heat at intermediate times. This is an empirical and arbitrary profile designed to test initial samples and to constrain optimal melting conditions.

Profile B (Figure 5(b)) is based on the shock-wave scenario for chondrule formation (Desch & Connolly 2002; Hood & Horanyi 1991; Wood 1996) and MM atmospheric entry (Rudraswami et al. 2016a). It is based on two Gaussian functions modeling relatively fast heating and a comparatively slower cooling.

Table 2
Chemical Composition of the Feldspar Precursor Material

| Sample Oxide | Feldspar Precursor (wt %) | Cations Calculated based on 32 Oxygen Atoms | |
|--------------------------------|---------------------------|---|-------|
| SiO ₂ | 67.15 | Si | 12.17 |
| Al ₂ O ₃ | 18.08 | Al | 3.86 |
| MnO | 0.03 | Mn | 0.01 |
| MgO | 0.07 | Mg | 0.02 |
| Fe ₂ O ₃ | 0.52 | Fe+3 | 0.08 |
| NaO | 2.93 | Na | 1.03 |
| CaO | 0.45 | Ca | 0.09 |
| TiO ₂ | 0.05 | Ti | 0.01 |
| K ₂ O | 10.05 | K | 2.32 |
| P ₂ O ₅ | 0.02 | P | 0.00 |
| PXC | 0.66 | | |
| Total | 100.00 | | |
| | | Ab % | 29.9 |
| | | An % | 2.5 |
| | | Or % | 67.5 |

Note. b.d. = below detection limit.

We are able to program arbitrary profiles, e.g., based on model scenarios for chondrule formation and MM atmospheric entry. In the future we plan to use a short heating phase with two different cooling phases, the second slower than the first, as derived from the chondrule formation scenario model proposed by Jones et al. (2017).

4. Results

We have fabricated samples similar to chondrules and MMs with our device Citlalmitl using different heating and cooling conditions with the two different laser power profiles (A and B), as explained above. We have carried out several

Table 3
Summary of Some Experimental Parameters^a

| Sample | Profile | Number Grains | Spot Radius (mm) | Duty Cycle max (%) | Power Pmax (W) | Intensity (W cm^{-2}) | Time | | | Cooling Rate ($^{\circ}\text{C h}^{-1}$) | Mass (mg) | | Diameter (μm) | | Temperature max ($^{\circ}\text{C}$) | Mass Loss ^b % |
|----------|------------|---------------|------------------|--------------------|----------------|----------------------------------|-------|--------|--------|--|-----------|-------|----------------------------|--------|--|--------------------------|
| | | | | | | | T (s) | t1 (s) | tm (s) | | Initial | Final | Initial | Final | | |
| 20_1-2b | plateau | 1 | 1.04 | 90 | 52.11 | 1.5×10^3 | 480 | 30 | 420 | 3.4×10^3 ^c | 0.75 | 0.45 | 759.46 | 643.64 | 1401 | 40.0 |
| 20_6-2bB | plateau | 1 | 1.04 | 90 | 52.11 | 1.5×10^3 | 540 | 30 | 480 | 1.3×10^3 ^c | 1.2 | 0.7 | 935.11 | 727.93 | 1382 | 41.7 |
| 23_5-1b | plateau | Few | 1.75 | 90 | 49.5 | 5.1×10^2 | 300 | 15 | 300 | 4.9×10^4 | ... | 0.35 | 125–250 ^d | 729 | 1303 | ... |
| 29_1-3 | shock wave | Few | 1.75 | 95 | 51.3 | 5.3×10^2 | 120 | ... | 10 | 1.5×10^4 | 0.33 | 0.29 | 618 ^e | 592 | 1501 | 12.1 |

Notes.

^a Profile, Time parameters, Power, and Duty cycle are related to Figure 5's laser profile arrangement.

^b Mass loss is due to ablation.

^c Cooling rates calculated with maximum temperature reached and the registered temperature at the end of the irradiation (see Figure 6).

^d Several grains with diameters between 125 μm and 250 μm were melted in one depression of the sample holder.

^e Diameter of the olivine grain.

experimental runs, with the different conditions summarized in Table 3. For all the experiments, the laser intensity modulation was used at a repetition rate of 5 kHz.

Our experimental device can reproduce any desired thermal history, as constrained by the laser's minimum rise and fall times. As examples, we present four of the samples created with Citlalmitl. Figure 6 shows both the programmed laser power profile and the resulting temperature profile for various cases. In the case of Figures 6(g) and (j), we have also shown the measured laser beam power versus time profile (these represent more recent experimental runs for which this capability had been added). Ideally, all three curves (programmed laser duty cycle, power measurement, and temperature measurement profiles) should exhibit the same trend.

In Table 4, we present the chemical composition of the experimental samples, which were obtained by analyses with a JEOL JXA 8900R electron probe microanalyzer (EPMA). Analyses were conducted at an accelerating voltage of 20 keV, with a beam current of 20 nA, a beam size of 1 μm , and a 40 s counting time. Natural phases of well-known compositions were used as standards.

Figures 6(a) and (b) show the backscattering images of a representative glassy sample (20_1-2b) created with the plateau profile A. We can see that the temperature profile and the programmed plateau profile follow the same trend (Figure 6(c)); this means that we were able to control the temperature behavior during irradiation. Sample 20_1-2b shows a semi-spherical shape and olivine crystals of skeletal type on the surface and glassy texture. In the cross-section image (Figure 6(b)), the relict grain and the iron oxides appear clearly. The relict grain composition is Fa 4.7 mol%, while on the rim of the melt it is Fa 2.4 mol% (Table 4).

In Figures 6(d) and (e) we show the backscattering images of a representative olivine sample (20_6-2bB), created with the plateau profile A. In Figure 6(d) it is seen that sample 20_6-2bB suffered a highly effective cooling mechanism and crystallized rapidly, resulting in a barred olivine texture, this could be explained by a high Fe evaporation rate that resulted in condensation and precipitation in the form of cubic iron oxides (white color in Figure 6(e)). Crystals in the core have a composition of Fa 3.7 mol% and in the rim the composition is of Fa 13.7 mol% (Table 4).

Figures 6(g) and (h) show sample 23_5-1b, irradiated with the profile A, with measurements of the laser power and sample temperature during the irradiation; they confirm our effective control over the temperature behavior during irradiation (Figure 6(i)). Sample 23_5-1b also shows Fe-rich minerals close to its surface and an important relict grain (Figures 6(g) and (h)). This sample used a few grains as a precursor, a single one of which melted (partially); in Figure 6(g) we have chosen to show the single coarse grain that exhibited melting. We have observed that in those cases for which the sample is in the form of a single grain, melting is more successful. According to Table 4, the relict grain composition is Fa 10.4 mol% and in the rim of the melt it is Fa 6.4 mol%.

Figures 6(j) and (k) show another representative sample (29_1-3) that was irradiated with shock-wave profile B, for which we have also included the power and temperature versus time measurements during the course of the irradiation (Figure 6(l)). Figure 6(l) shows the similarity between the programmed shock-wave profile, the laser beam power measurements, and the temperature behavior. This sample

was formed with a combination of fine feldspar grains and one coarse olivine grain resulting in elongated radial pyroxene bars and glass material on its surface and its cross section. The Fs content in the core is 9.4 mol% and near the surface it is 10.5 mol% (Table 4).

5. Discussion

It has been noted that the peak temperature and cooling rate control the melting and heat loss of an igneous system, and in turn determine the resulting textures of meteoritic material (Radomsky & Hewins 1990; Connolly & Jones 2016; van Ginneken et al. 2017). For example, chondrules are associated with cooling rates within the range 0.5 to $3 \times 10^3 \text{ }^\circ\text{C h}^{-1}$, with partially melted (porphyritic chondrules) resulting for the lower cooling rates and completely melted chondrules (barred olivine and radial pyroxene-like chondrules) resulting for the higher cooling rates (Desch et al. 2012). Micrometeorite cooling rates are of the order of 10^4 – $10^5 \text{ }^\circ\text{C h}^{-1}$ depending on the entry angle of the precursor (Rudraswami et al. 2016a; Wilson et al. 2019). The specific combination of peak temperature and precursor grain size (coarse or fine grained) determines the survival of crystallization nuclei and thus the formation of barred textures (e.g., van Ginneken et al. 2017).

In our experimental runs all precursors are coarse-grained and cooling rates range from $1.3 \times 10^3 \text{ }^\circ\text{C h}^{-1}$ to $4.9 \times 10^4 \text{ }^\circ\text{C h}^{-1}$ (Table 3). Some of our first experimental runs presented in this paper using Citlalmitl allow us to test our temperature control over the samples by controlling the laser duty cycle. Given the same irradiation profile, longer irradiation profiles (T in Table 3 and Figure 5) imply less accurate control over the temperature; this is shown by the agreement between measured temperature and programmed profile (black and blue lines in Figures 6(c)–(l)). In all cases, higher duty cycles produce larger peak temperatures (Table 3).

Other factors may influence the absorption efficiency of the precursors that we are so far not able to fully control during the experiments, for example: the crystallographic orientation of the precursor grains, the exact position of the grain in the depression of the sample holder, and the gas retained inside the precursor grains.

The experimental conditions of samples 20_1-2b and 20_6-2bB are very similar to each other, resulting in similar mass losses, but different textures (Figure 6(d) and Table 3) as a result of different cooling rates. Sample 20_1-2b (Figure 6(a)) have a clear relict grain, indicating partial melting; the general texture of the sample is similar to a CC micrometeorite (e.g., Figure 1 sample G in Genge et al. 2017 sample 445 in Larsen 2017 Figure 1 sample #10.17 in van Ginneken et al. 2017) or glassy-rich olivine chondrule (e.g., Figure 10 in Radomsky & Hewins 1990). Sample 20_6-2bB resulted in a barred texture (Figure 6(d)) that can be compared with a BO chondrule or MM (e.g., Figure 3 in Radomsky & Hewins 1990, Figure 2 sample i in Lauretta et al. 2006, and Figure 1 sample h in Folco & Cordier 2015). This sample shows Fe enrichment close to the rim in two forms: in the silicate composition (Table 4) and in an increase of Fe oxide particles. Both samples 20_1-2b and 20_6-2bB lost iron in general, but some iron was deposited in oxide form over the surface or between the crystals.

Samples 23_5-1b and 29_1-3 were irradiated under similar experimental conditions, except for the irradiation profile and initial number of grains (see Table 3), which resulted in two

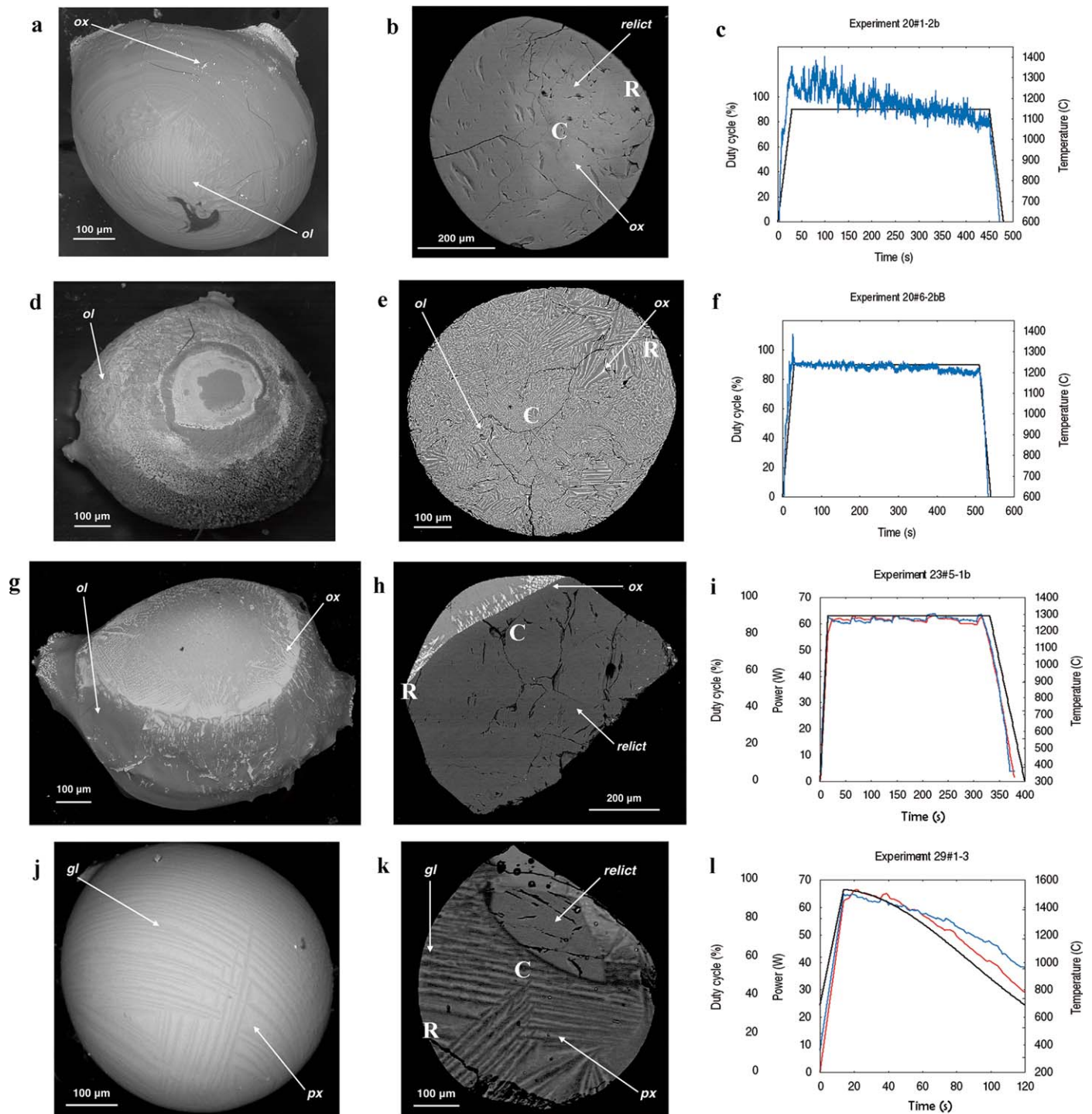


Figure 6. (a) Experiment 20_1-2b. Sample created with the plateau irradiation profile (A). The backscattering electron image shows in medium gray color molten olivine and in white some metal oxides. (b) Cross-section image that shows glassy texture and the relict grain and oxides in white. (c) Temperature measurements (blue line) and duty cycle programmed profile (black line). (d) Experiment 20_6-2bB. Olivine sample created with profile A. The backscattering electron image shows in medium gray barred olivine. (e) Cross-section image that shows in medium gray olivine bars and in white color Fe-rich oxides. (f) Plot lines as described in (c). (g) Experiment 23_5-1b. Sample created with profile A, with laser beam power measurement. White is iron oxide and light gray shows partially molten olivine. (h) Cross-section image that shows Fe oxides in white, glass in gray, and in dark gray a relict olivine crystal. (i) Temperature measurements (blue line), duty cycle programmed profile (black line) and laser beam power measurement (red line). (j) Experiment 29_1-3. Sample created with the shock-wave irradiation profile (B), with laser beam power measurement. The light gray is elongated multiple radial crystals and medium gray is interstitial glass. (k) Cross-section image that shows the relict grain; glass in gray and radial pyroxene in medium gray. (l) Plot lines as described in (i). The parameters used for all experiments are shown in Table 3. *C* = analyzed point in the core of the sample shown in Table 4. *R* = analyzed point in (or close to) the rim of the sample shown in Table 4.

different morphologies and textures (Figures 6(g) and (j)). For run 23, several grains were placed in each depression of the sample holder. The exact number cannot be controlled due to

the small diameters of the grains (125 μm to 250 μm). The result was a partially molten sample with a flatter shape compared with that shown in Figure 6(j). Sample 23_5-1b

Table 4
Chemical Composition of the Experimental Samples Obtained by EPMA Analyses

| Sample | 20_1-2b | | 20_6-2bB | | 23_5-1 | | 29_1-3 | | |
|--------------------------------|---------|--------|----------|---------|---------|---------|--------|---------|------|
| | core | rim | core | rim | Core | Rim | Core | Rim | |
| SiO ₂ | 40.949 | 41.126 | 41.543 | 40.001 | 45.745 | 39.810 | 54.313 | 55.150 | |
| Al ₂ O ₃ | 0.007 | 0.008 | n.d. | 0.027 | n.d. | n.d. | 3.222 | 7.820 | |
| MnO | 0.080 | 0.070 | 0.061 | 0.205 | n.d. | n.d. | n.d. | n.d. | |
| MgO | 53.177 | 55.478 | 52.950 | 47.139 | 44.954 | 53.660 | 34.367 | 29.700 | |
| FeO | 4.684 | 2.378 | 3.585 | 13.390 | 9.302 | 6.530 | 6.336 | 6.220 | |
| Na ₂ O | n.d. | n.d. | n.d. | 0.025 | n.d. | n.d. | n.d. | n.d. | |
| CaO | 0.016 | 0.013 | 0.011 | 0.147 | n.d. | n.d. | n.d. | n.d. | |
| TiO ₂ | 0.003 | n.d. | n.d. | n.d. | n.d. | n.d. | n.d. | n.d. | |
| K ₂ O | 0.029 | 0.024 | n.d. | n.d. | n.d. | n.d. | 1.761 | 1.110 | |
| NiO | 0.458 | 0.175 | 0.355 | 0.420 | n.d. | n.d. | n.d. | n.d. | |
| Total | 99.403 | 99.272 | 98.505 | 101.354 | 100.001 | 100.000 | 99.999 | 100.000 | |
| Si | 0.989 | 0.984 | 1.005 | 0.987 | 1.100 | 0.965 | 1.895 | 1.898 | |
| Al | n.d. | n.d. | n.d. | 0.001 | n.d. | n.d. | 0.132 | 0.317 | |
| Mn | 0.002 | 0.001 | 0.001 | 0.004 | n.d. | n.d. | n.d. | n.d. | |
| Mg | 1.915 | 1.979 | 1.909 | 1.733 | 1.612 | 1.938 | 1.787 | 1.524 | |
| Fe | 0.095 | 0.048 | 0.073 | 0.276 | 0.187 | 0.132 | 0.185 | 0.179 | |
| Na | n.d. | n.d. | n.d. | 0.001 | n.d. | n.d. | n.d. | n.d. | |
| Ca | n.d. | n.d. | n.d. | 0.004 | n.d. | n.d. | n.d. | n.d. | |
| Ti | n.d. | n.d. | n.d. | n.d. | n.d. | n.d. | n.d. | n.d. | |
| K | 0.001 | 0.001 | n.d. | n.d. | n.d. | n.d. | 0.078 | 0.049 | |
| Ni | 0.009 | 0.003 | 0.007 | 0.008 | n.d. | n.d. | n.d. | n.d. | |
| Fo% | 95.3 | 97.7 | 96.3 | 86.3 | 89.6 | 93.6 | En% | 90.6 | 89.5 |
| Fa% | 4.7 | 2.4 | 3.7 | 13.7 | 10.4 | 6.4 | Fs% | 9.4 | 10.5 |

Note. n.d. = nondetected.

bears a similarity to a partially molten semi-spherical MM. The precursor of sample 29_1-3 was a single olivine grain attached with some fine feldspar grains (composition in Table 2), and was irradiated with a shock-wave type thermal history, which resulted in an almost fully melted sample (Figure 6(j)), with an interesting texture that could be classified as an RP-like chondrule, considering that the properties of the resulted pyroxene are different because of the olivine precursor (Table 4). Table 4 shows that the composition of our samples could be compared with some type IA chondrules in Semarkona and Allende (e.g., Alexander et al. 2008; Simon & Haggerty 1979) and some Antarctic collections of MMs (e.g., Imae et al. 2013). Additionally, the presence of some relict grains in our samples is similar to those reported for chondrules and MMs (e.g., Figure 9 in Taylor et al. 2012).

Regarding the profiles, Profile A is an empirical and arbitrary profile designed to test samples and it has no physical interpretation, as we mentioned above. Indeed, profile A does not represent realistic sample-formation conditions. It helped us to determine whether we could control certain experimental parameters, including the heating and cooling rates. In the future we will concentrate on developing more realistic profiles.

There are multiple ways in which Citlalmitl could be improved. First, we mention the future implementation of a system designed for measuring the spectrum of the infrared radiation from the sample during irradiation, yielding spectrally resolved thermal histories. Second, we mention other possible applications for this device, such as the reproduction of chondrule analogs in more realistic environments; we could conduct experiments in different atmospheres, so as to, for example, mimic the solar nebula H₂ environment where chondrule formation took place. Other important possible

applications are the reproduction of chondrule and MM analogs with more realistic compositions for precursors, the replication of the melting crust of meteorites, the study of MM ablation, and laser-induced plasmas for the study of lightning in different atmospheres.

6. Conclusions

We have designed and implemented a new experimental device, which we have named Citlalmitl, to reproduce chondrules and MMs using a 50W CO₂ laser beam taking advantage of laser irradiation versus the use of other competing methods. The most important advantage of Citlalmitl is that it is able to control the optical intensity reaching the sample, through the ability to program specific irradiation temporal profiles to mimic the thermal conditions predicted by the models for chondrules and MM formation. With this new device, in addition to being able to set the power versus temperature profile, we can directly measure the thermal history (sample temperature versus time) during the irradiation process. While we have carried out experimental runs with two different types of optical power profiles (plateau and shock wave), we emphasize our ability to program arbitrary profiles in our device.

K.C. is thankful for support from the grant UNAM-PAPIIT IN117619. P.H.-R. acknowledges the support from Conacyt scholarship number 301412. A.U. acknowledges support from PAPIIT (UNAM) grant IN104418, CONACYT Fronteras de la Ciencia grant 1667, and AFOSR grant FA9550-16-1-1458. The authors thank José Rangel for manufacture assistance; Carlos Linares from Laboratorio Universitario de Petrología-LAN-GEM in Instituto de Geofísica, UNAM; Sonia Ángeles and María del Consuelo Macías from Instituto de Geología, UNAM

for technical assistance; Gabriela Solís and Teodoro Hernández from LUGIS in Instituto de Geofísica, UNAM; Claudia Camargo and Dr. Negrón from the Chemical Evolution Laboratory at ICN, UNAM; and Taller de Mineralogía y Petrología from Departamento de Física, Facultad de Ciencias, UNAM for letting us use their instruments. We specially thank the reviewers for their helpful comments.

ORCID iDs

Patricia Hernández-Reséndiz  <https://orcid.org/0000-0003-3988-7289>

Alfred B. U'Ren  <https://orcid.org/0000-0002-4963-9388>

Karina Elizabeth Cervantes-de la Cruz  <https://orcid.org/0000-0002-0089-9023>

Antígona Segura  <https://orcid.org/0000-0002-2240-2452>

References

- Alexander, C. M. O., Grossman, J. N., Ebel, D. S., & Ciesla, F. J. 2008, *Sci*, **320**, 1617
- Badjukov, D. D., Brandstätter, F., Raitala, J., & Kurat, G. 2010, *M&PS*, **45**, 1502
- Battandier, M., Bonal, L., Quirico, E., et al. 2018, *Icar*, **306**, 74
- Blander, M., Planner, H. N., Keil, K., Nelson, L. S., & Richardson, N. L. 1976, *GeCoA*, **40**, 889
- Borucki, W. J., Giver, L. P., McKay, C. P., Scattergood, T., & Parris, J. E. 1988, *Icar*, **76**, 125
- Borucki, W. J., Kenzie, R. L. M., McKay, C. P., Duong, N. D., & Boac, D. S. 1985, *Icar*, **64**, 221
- Bowey, J. E., Adamson, A. J., & Whittet, D. C. B. 1998, *MNRAS*, **298**, 131
- Briani, G., Pace, E., Shore, S. N., et al. 2013, *A&A*, **552**, A53
- Brownlee, D. E., Bates, B., & Beauchamp, R. H. 1983, *Chondrules and Their Origins* (Houston, TX: Lunar and Planetary Institute), 10
- Cervantes-de la Cruz, K. E. 2009, *Estudio Petrológico de los Condros de las Meteoritas Condriticas Mexicanas Cuartaparte, Cosina, y Nuevo Mercurio: Origen y Evolución de Dichas Estructuras* (Mexico City: UNAM)
- Cervantes-de la Cruz, K. E., Segura, A., & Ortega-Gutiérrez, F. 2015, *LPICo*, **1856**, 5380
- Ciesla, F. J. 2005, in *Proc. ASP Conf. Ser. 341, Chondrites and the Protoplanetary Disk*, ed. A. N. Krot, E. R. D. Scott, & B. Reipurth (San Francisco, CA: ASP), 811
- Connolly, H. C., & Jones, R. H. 2016, *JGRE*, **121**, 1885
- Desch, S. J., & Connolly, H. C., Jr. 2002, *M&PS*, **37**, 183
- Desch, S. J., Morris, M. A., Connolly, H. C., & Boss, A. P. 2012, *M&PS*, **47**, 1139
- Eisenhour, D. D., Daulton, T. L., & Buseck, P. R. 1994, *Sci*, **265**, 1067
- Engrand, C., Duprat, J., Bardin, N., et al. 2016, *IAUFM*, **29**, 253
- Farmer, V. C. 1976, *MinM*, **40**, 540
- Ferus, M., Nesvorný, D., Šponer, J., et al. 2015, *PNAS*, **112**, 657
- Folco, L., & Cordier, C. 2015, *EMU Notes in Mineralogy*, **15**, 253
- Genge, M. J. 2017, *M&PS*, **52**, 1000
- Genge, M. J., Engrand, C., Gounelle, M., & Taylor, S. 2008, *M&PS*, **43**, 497
- Genge, M. J., Grady, M. M., & Hutchison, R. 1997, *GeCoA*, **61**, 5149
- Genge, M. J., Larsen, J., Ginneken, M. V., & Suttle, M. D. 2017, *Geo*, **45**, 119
- Gooding, J. L., & Keil, K. 1981, *Metic*, **16**, 17
- Gounelle, M., Chaussidon, M., Morbidelli, A., et al. 2009, *PNAS*, **106**, 6904
- Greshake, A., Kloeck, W., Arndt, P., et al. 1998, *M&PS*, **33**, 267
- Hewins, R. H., Jones, R. H., & Scott, E. R. D. 1996, in *Proc. Int. Chondrules and the Protoplanetary Disk Conf.* (Cambridge: Cambridge Univ. Press)
- Hewins, R. H., & Fox, G. E. 2004, *GeCoA*, **68**, 917
- Hewins, R. H., Radomsky, P. M., & Connolly, H. C., Jr. 1989, *LPI*, **20**, 412
- Hood, L. L., & Horanyi, M. 1991, *Icar*, **93**, 259
- Imae, N., Taylor, S., & Iwata, N. 2013, *GeCoA*, **100**, 116
- Jones, R. H. 1994, *GeCoA*, **58**, 5325
- Jones, R. H. 2012, *M&PS*, **47**, 1176
- Jones, R. H., Villeneuve, J., & Libourel, G. 2017, *LPICo*, **1963**, 2029
- Kaluna, H. M., Ishii, H. A., Bradley, J. P., Gillis-Davis, J. J., & Lucey, P. G. 2017, *Icar*, **292**, 245
- Larsen, J. 2017, *In Search of Stardust: Amazing Micrometeorites and Their Terrestrial Imposters* (Beverly, MA: Voyageur Press)
- Lauretta, D. S., Nagahara, H., & Alexander, C. M. O'D. 2006, in *Meteorites and the Early Solar System II*, ed. D. S. Lauretta & H. Y. McSween, Jr. (Tucson, AZ: Univ. Arizona Press), 431
- Lofgren, G. 1989, *LPICo*, **698**, 56
- Lofgren, G., & Lanier, A. B. 1990, *GeCoA*, **54**, 3537
- McSween, H. Y. 1977, *GeCoA*, **41**, 1843
- Mvondo, D. N., Navarro-González, R., McKay, C. P., Coll, P., & Raulin, F. 2001, *AdSpr*, **27**, 217
- Nagashima, K., Tsukamoto, K., Satoh, H., Kobatake, H., & Dold, P. 2006, *JCrGr*, **293**, 193
- Nakamura, T., Noguchi, T., Tsuchiyama, A., et al. 2008, *Sci*, **321**, 1664
- Nelson, L. S., Blander, M., Skaggs, S. R., & Keil, K. 1972, *E&PSL*, **14**, 338
- Nesvorný, D., Jenniskens, P., Levison, H. F., et al. 2010, *ApJ*, **713**, 816
- Nordine, P. C., & Atkins, R. M. 1982, *RSci*, **53**, 1456
- Oliveira, I., Olofsson, J., Pontoppidan, K. M., et al. 2011, *ApJ*, **734**, 51
- Ostrooumov, M. 2007, *Espectrometría Infrarroja de Reflexión en Mineralogía Avanzada. Geomología y Arqueometría* (Mexico City: UNAM)
- Poppe, T., Güttler, C., & Springborn, T. 2010, *EP&S*, **62**, 53
- Radomsky, P. M., & Hewins, R. H. 1990, *GeCoA*, **54**, 3475
- Ramírez, S. I., Navarro-González, R., Coll, P., & Raulin, F. 2005, *AdSpr*, **36**, 274
- Rubin, A. E., & Grossman, J. N. 2010, *M&PS*, **45**, 114
- Rudraswami, N. G., Prasad, M. S., Dey, S., et al. 2016a, *ApJ*, **831**, 197
- Rudraswami, N. G., Prasad, M. S., Dey, S., et al. 2016b, *ApJS*, **227**, 15
- Scattergood, T. W., McKay, C. P., Borucki, W. J., et al. 1989, *Icar*, **81**, 413
- Scott, E. R. D. 2007, *AREPS*, **35**, 577
- Scott, E. R. D., & Taylor, G. J. 1983, *JGRS*, **88**, B275
- Simon, S. B., & Haggerty, S. E. 1979, *LPI*, **10**, 871
- Solé, J. 2009, *RCMS*, **23**, 3579
- Soulié, C., Libourel, G., & Tissandier, L. 2017, *M&PS*, **52**, 225
- Sturm, B., Bouwman, J., Henning, T., et al. 2013, *A&A*, **553**, A5
- Taylor, S., Matrajt, G., & Guan, Y. 2012, *M&PS*, **47**, 550
- Toppani, A., Libourel, G., Engrand, C., & Maurette, M. 2001, *M&PS*, **36**, 1377
- Toppani, A., Marty, B., Zimmermann, L., & Libourel, G. 2003, *LPI*, **34**, 2028
- Tsuchiyama, A., & Nagahara, H. 1981, *PolRe*, **20**, 175
- Tsuchiyama, A., Nagahara, H., & Kushiro, I. 1980, *E&PSL*, **48**, 155
- van Ginneken, M., Gattacceca, J., Rochette, P., et al. 2017, *GeCoA*, **212**, 196
- Villagran-Muniz, M., Sobral, H., Navarro-Gonzalez, R., Velazquez, P. F., & Raga, A. C. 2003, *PPCF*, **45**, 571
- Weisberg, M. K., McCoy, T. J., & Krot, A. N. 2006, in *Meteorites and the Early Solar System II*, ed. D. S. Lauretta & H. Y. McSween, Jr. (Tucson, AZ: Univ. Arizona Press), 19
- Wilson, A. P., Genge, M. J., Krzesinska, A. M., & Tomkins, A. G. 2019, *M&PS*, **54**, 1
- Wood, J. A. 1996, *M&PS*, **31**, 641
- York, D., Hall, C. M., Yanase, Y., Hanes, J. A., & Kenyon, W. J. 1981, *GeoRL*, **8**, 1136
- Zhu, C., Góbi, S., Abplanalp, M. J., et al. 2020, *NatAs*, **4**, 45